npj | clean water

www.nature.com/npjcleanwater

ARTICLE OPEN

Check for updates

Heavy metal and organic dye removal via a hybrid porous hexagonal boron nitride-based magnetic aerogel

A. Santhana Krishna Kumar[1,2], Jolanta Warchol[3], Jakub Matusik[2], Wei-Lung Tseng[1,4]✉, N. Rajesh[5]✉ and Tomasz Bajda[2]✉

Numerous adsorbents have been introduced to efficiently remove heavy metals and organic dyes from environmental water samples. However, magnetic a porous network aerogels are rarely developed to capture inorganic and organic pollutants from aqueous. We herein fabricated hexagonal boron nitride nanosheets (*h*-BNNSs)-based on magnetic hybrid aerogels (MHAs) as a lightweight adsorbent for robust uptake of Cr(VI), As(V), methylene blue (MB) and acid orange (AO). The synthetic procedure of poly(ethyleneimine)-modified *h*-BNNSs (PEI-*h*-BNNSs) involved thermal poly condensation of melamine and boric acid, pyrolysis of the resultant products which allowed exfoliated by ultra-sonication process further functionalization with PEI-mediated modification of *h*-BNNSs. The as formed PEI-*h*-BNNSs allowed in-situ formation of magnetite nanoparticles (Fe_3O_4 NPs) decorated on their surfaces, which are turned to be PEI-*h*-BNNSs@Fe_3O_4 NPs. The lyophilization treatment of PEI-*h*-BNNSs@Fe_3O_4 NPs-loaded PVA hydrogels generated the MHAs with large porous structures, diverse and numerous functional groups, good super-paramagnetic and a zero net surface charge. These features enabled the proposed adsorbent (MHAs) to be utilized to efficiently remove Cr(VI), As(V), MB, and AO from an aqueous solution, with maximum adsorption capacity estimated to be 833, 426, 415, 286 mg g^{-1}, respectively. The adsorption kinetics and isotherm data demonstrated that MHAs mediated adsorption of Cr(VI), As(V), MB and AO followed the Freundlich isotherm model and a pseudo-second-order kinetics model. This finding signifies that the MHAs exhibit heterogeneous binding behavior with multilayer chemisorption of Cr(VI), As(V), MB and AO. Subsequently, the practical application were validated by conducting their detoxification of chromium and arsenic in soli-sludge samples.

npj Clean Water (2022)5:24; https://doi.org/10.1038/s41545-022-00175-0

INTRODUCTION

Rapid urbanization and industry expansion have caused massive increases in inorganic and organic pollutants in natural water, which are heavily connected with public health and water quality[1–3]. Various industries discharge their heavy metals, organic dyes and poly cyclic aromatic hydrocarbons (PAH) into the aquatic systems without a proper purification process from among those pollutants. The removal of toxic metals[1–3], organic dyes[4] and poly cyclic aromatic hydrocarbons (PAH)[5–8] from environmental waters have recently been regarded as one of the most essential issues to obtaining clean water due to their environmental persistency and extreme toxicity. In response to this requirement, several procedures have been introduced to purify heavy metals and organic dye-polluted water, including photo-catalysis[9], flocculation[10], biodegradation[11], membrane separation[12], and adsorption[13] techniques. Among them adsorption-related methods have been intensively utilized to remove different pollutants due to their cost-effective operation, high capture efficiency and very limited secondary pollutions are created. To identifying an appropriate adsorbent is expected to fulfill the following criteria: (1) high adsorption capability for diverse pollutants at low concentrations; (2) excellent reusability without sacrificing surface binding sites; (3) fast adsorption rate in complex matrices.

According to the above principles, numerous adsorbents have been proposed to remediate environmental pollutants, exemplified by activated carbon[14], graphene oxide-based composites[15], synthetic polymers[16], co-ordination polymers[17], metal-organic frameworks[18], covalent organic framework[19], and surfactant-anchored biopolymer[20]. Recently, hexagonal boron nitride (*h*-BN) displays a promising alternative for capturing environmental pollutants owing to its highly porous structure, polar B–N bonds, and sp^2 hybridization. The reported *h*-BN-related materials include BN spheres[2], *h*-BN whiskers[21], BN nanosheets (BNNSs)[22], cheese-like 3D BN[23], chemically activated BN fibers[24] and BN hollow spheres[25]. Moreover, introducing a suitable agents can functionalize through their *h*-BN surface with specific groups can efficiently interacting with adsorbates. This synergistic effect enables the *h*-BN-related adsorbents to have multiple binding sites to interact with diverse environmental pollutants[26–28]. As an example of heavy metals sorption, the polar B–N bonds obtained from *h*-BN-related materials could electrostatically attract toxic metal cations through their surface, such as Cr(III)[1–3,27], Cu(II)[1,2], and Pb(II)[1–3]. Moreover, the *h*-BN-based porous materials exfoliated with polyaniline further decorated by magnetite nanoparticles (Fe_3O_4 NPs) were well-suited for the uptake of Cr(VI)[26] and As(V)[28], respectively. In another example, the *h*-BN-related porous adsorbent can efficiently remove cationic and anionic dyes from environmental water through their π-π interactions, structural defects and polar B–N bonds[1–3,21–25]. Although recent literature studies shows the potential behavior to remove environmental pollutants from an aqueous system, these BN-based porous adsorbents suffer from insufficient adsorption capacity due to

[1]Department of Chemistry, National Sun Yat-sen University, No. 70, Lien-hai Road, Gushan District, Kaohsiung 80424, Taiwan. [2]Department of Mineralogy, Petrography and Geochemistry, Faculty of Geology, Geophysics and Environmental Protection, AGH University of Science and Technology, Al. Mickiewicza 30, 30-059 Krakow, Poland. [3]Department of Advanced Material Technology, Faculty of Chemistry, Wroclaw University of Science and Technology, ul. M. Smoluchowskiego 25, Wroclaw 50-372, Poland. [4]School of Pharmacy, Kaohsiung Medical University, No. 100, Shiquan 1st Road, Sanmin District, Kaohsiung 80708, Taiwan. [5]Department of Chemistry, Birla Institute of Technology and Science, Pilani-Hyderabad Campus, Jawahar Nagar, Shameerpet Mandal, Hyderabad 500 078, India. ✉email: tsengwl@mail.nsysu.edu.tw; nrajesh@hyderabad.bits-pilani.ac.in; bajda@agh.edu.pl

their hydrophobic nature and low surface-to-volume ratio. It is worth mentioning that the maximum adsorption capacity values of those above-discussed adsorbents were reported to be 10–133 mg g^{-1} for Cr(VI)[26], 10–30 mg g^{-1} for As(V)[28] and 10–392 mg g^{-1} for methylene blue (MB)[2,22–25], in sequence.

In response to this obstacle, our current study aimed to synthesize magnetic hybrid aerogels (MHAs) for efficiently capturing Cr(VI), As(V), MB and acid orange (AO) from an aqueous solution. The MHAs were prepared by "in situ" formation of magnetite nanoparticles (Fe_3O_4 NPs) onto the surface of polyethyleneimine-modified *h*-BNNSs (named PEI-*h*-BNNSs@Fe_3O_4 NPs), followed by sol-gel process and lyophilization treatment. The as-made MHAs (PEI-*h*-BNNSs@Fe_3O_4 NPs-loaded PVA aerogels) exhibited a three-dimensional structure with diverse functional groups (−N, − NH, − NH_2, and −OH), a large surface area to volume ratio and zero net charge. Additionally, incorporating magnetic material into aerogels had the added advantages of simplicity, low cost and rapidity in the recycling process. The solution pH was shown to be a determining factor for evaluating adsorption−desorption process of the adsorbents. The adsorption behavior of MHAs was addressed further by using adsorption isotherm and kinetic studies and their feasibility was demonstrated by remediating Cr(VI)/As(V)-contaminated soil sludge samples.

RESULTS

Fabrication and characterization of the *h*-BNNS-related nanomaterials and aerogels

Figure 1 illustrates the synthetic procedure for the PEI-*h*-BNNSs, PEI-*h*-BNNSs@Fe_3O_4 NPs, and MHAs. Previous studies have demonstrated that planar melamine molecules have three amino groups, forming hydrogen bonds with boric acid[29,30]. The formed hydrogen-bonded molecular frameworks can serve as a precursor to obtain *h*-BN whiskers[30]. Accordingly, this study prepared the *h*-BN whiskers via thermal poly-condensation of melamine and boric acid, followed by pyrolysis[31]. After exfoliating the *h*-BN whiskers with ultra-sonication, the resultant *h*-BNNSs were modified with PEI to enhance dispersity and adsorption capability. It is noted that the functionalization of PEI on the *h*-BNNS surface is attributable to Lewis acid-base interaction[32]. We next incorporated the as-developed PEI-*h*-BNNSs into the base-mediated co-precipitation of Fe (III) and Fe (II). Considering that a lone pair of electrons from a nitrogen atom can coordinate with Fe (III) and Fe (II)[33], the Fe_3O_4 NPs were in-suit formed on the PEI-*h*-BNNS surface. Electron microscopy techniques and Raman spectroscopy were implemented to characterize the as-prepared PEI-*h*-BNNSs. Figure 2a, b displays the low-magnification transmission electron microscopy (TEM) images of PEI-*h*-BNNSs, demonstrating the formation of 100–200 nm-sized nanosheets with a smooth surface. The atomic inter-planar distance of the PEI-*h*-BNNSs in the high-resolution TEM image reveals their inter-planar spacing of 0.33 nm (Fig. 2c), which is indexed to the (002) plane of *h*-BN crystals. The selected area electron diffraction (SAED) of the PEI-*h*-BNNSs shows multiple diffraction rings, reflecting their polycrystalline nature (Fig. 2d). The thickness of the PEI-*h*-BNNS, estimated by line profiles from atomic force microscopy (AFM) image, was less than 2 nm (inset in Fig. 2e). The layer number of PEI-*h*-BNNS was suggested to be nearly 6 according to the theoretical interlayer distance of *h*-BN corresponding to 0.34 nm. The aggregated spots in the AFM image could result from the increased interaction among the PEI-*h*-BNNSs during the sample evaporation[33]. The analyses from *h*-BN whiskers, PEI-*h*-BNNSs and PEI-*h*-BN quantum dots by Raman spectroscopy reveals that the characteristic D band at 1376 cm^{-1} (Fig. 2f), which is assigned to E_{2g} vibration mode of *h*-BN[34–37]. The full width at half maximum of an identified D band was determined to be approximately 10 cm^{-1}, reflecting that the above-mentioned materials possess a high-crystalline structure[38,39]. Additionally, the Raman intensity of the D band in these BN-related porous materials following the order: *h*-BN whiskers > PEI-*h*-BNNSs > PEI-*h*-BN quantum dots. Given that, Raman intensity of the D band is proportional to the layer number of *h*-

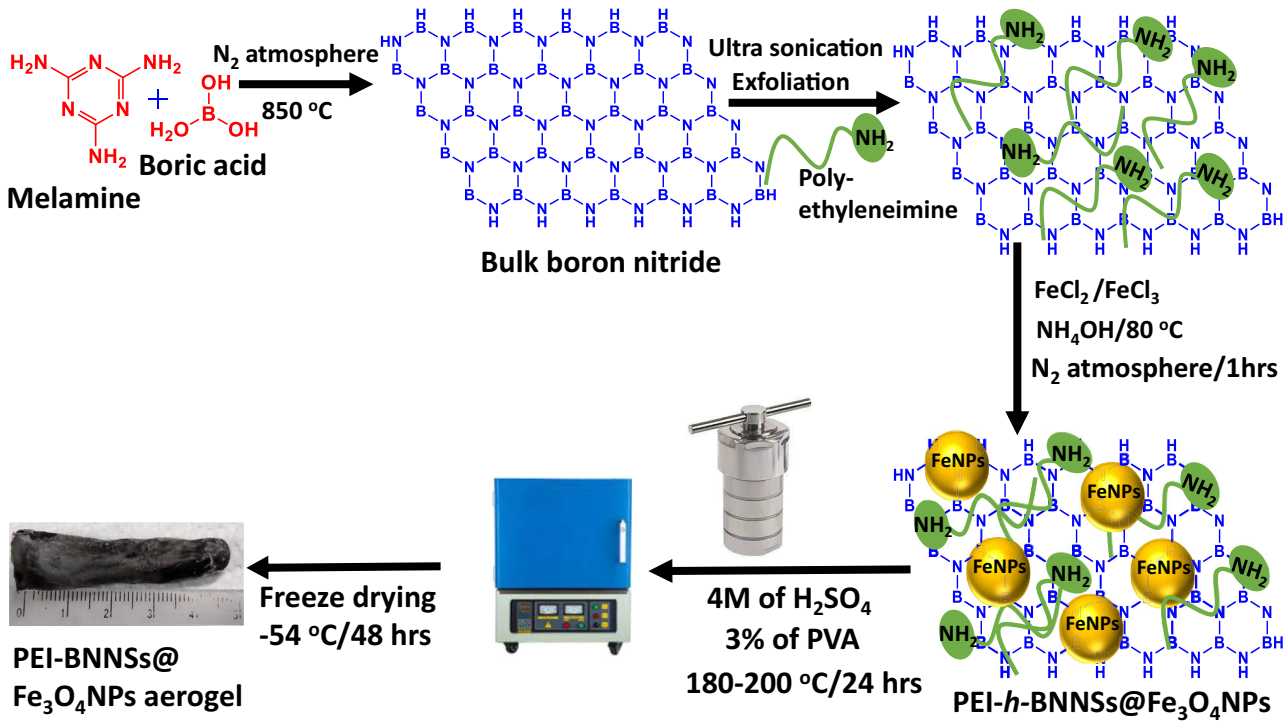

Fig. 1 Adsorbent preparation. The schematic illustration of detailed procedure for synthesis of magnetic hybrid aerogel (PEI-*h*-BNNSs@Fe_3O_4 NPs).

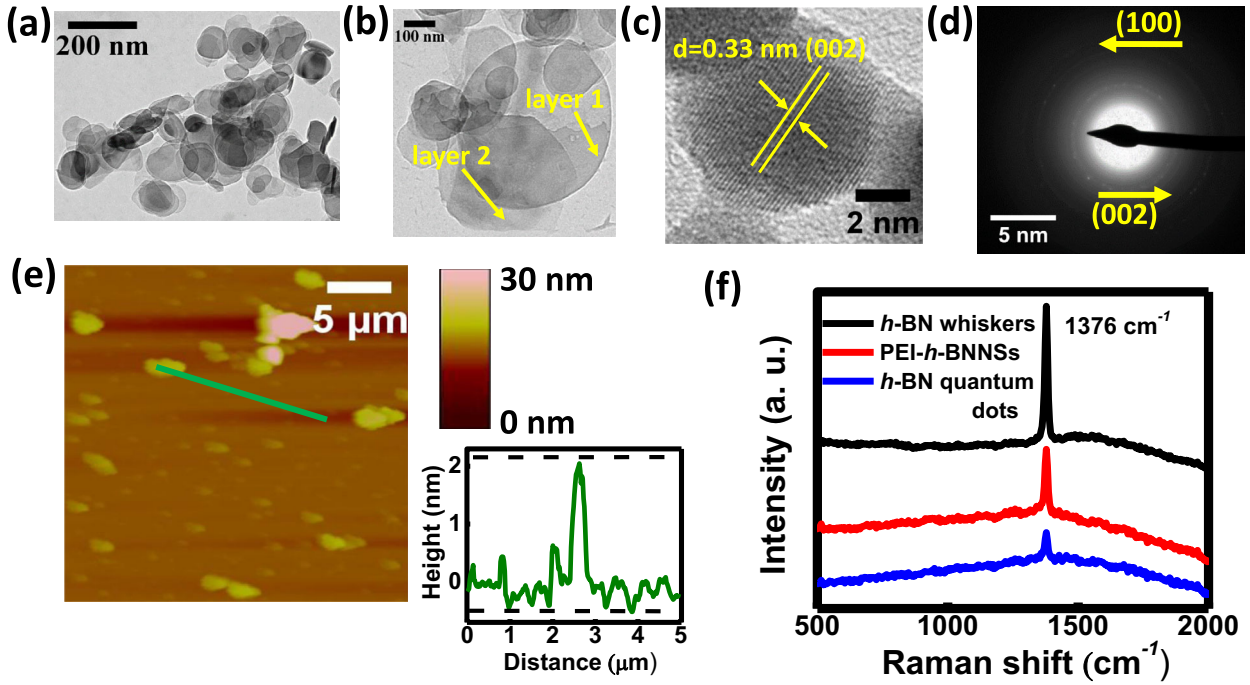

Fig. 2 Morphological and spectroscopic studies. Characterization of the PEI-*h*-BNNSs: **a**, **b** Low-magnification of TEM images, **c** high-resolution of TEM image, **d** SAED pattern, **e** AFM image and height profile (green line), and **f** Raman spectra (red line). The black and blue lines are (**f**) correspond to the Raman spectra of *h*-BN whiskers and *h*-BN quantum dots, respectively.

BN[38,39], we point out that the as-prepared PEI-*h*-BNNSs are indeed and exfoliated to few-layer structures.

In the subsequent study, we confirmed the formation of PEI-*h*-BNNSs@Fe_3O_4NPs and compared them with PEI-*h*-BNNSs and Fe_3O_4 NPs. The low-magnification TEM images of PEI-*h*-BNNSs@Fe_3O_4 NPs reveal that numerous spherical Fe_3O_4 NPs were attached to the edges of PEI-*h*-BNNSs (Fig. 3a, b). As shown in the corresponding high-resolution TEM image of Fig. 3c, the PEI-*h*-BNNSs@Fe_3O_4 NPs exhibited distinct lattice fringes with d-spacing of 0.33 and 0.21 nm corresponding to the (002) and (100) lattice planes of *h*-BNNSs (Fig. 3c) and cubic Fe_3O_4 NPs (Supplementary Fig. 1), respectively. The SAED ring pattern of PEI-*h*-BNNSs@Fe_3O_4 NPs reflects their polycrystalline structure (Fig. 3d). Moreover, the chemical composition of PEI-*h*-BNNSs@Fe_3O_4 NPs was evidenced by TEM equipped with energy dispersive spectroscopy (EDS). The EDS spectrum of PEI-*h*-BNNSs@Fe_3O_4 NPs displayed a series of peaks which corresponding to B, N, O and Fe elements (Fig. 3e). These observations confirm that the Fe_3O_4 NPs could be in situ formed on the PEI-*h*-BNNS surface edges through their direct binding of Fe(II) and Fe(III) with the PEI-*h*-BNNSs[28,40,41]. The X-ray diffraction (XRD) technique was utilized to support the formation of composites PEI-*h*-BNNSs@Fe_3O_4 NPs and Fe_3O_4 NPs. Because of the crystalline behavior of PEI-*h*-BNNSs@Fe_3O_4 NPs, which provides two intense XRD peaks at 2θ angles of 27.9° and 30.3°corresponded to the (002) planes of *h*-BN whiskers[28,40,41] and (220) plane of cubic Fe_3O_4 NPs[28,40], respectively (Fig. 3f). A comparison between the main XRD peak of PEI-*h*-BNNSs@Fe_3O_4 NPs and that of the PEI-h-BNNSs@Fe_3O_4 NPs has a slight difference in the 2θ angle value, a similar result were also detected in the XRD measurement of Fe_3O_4 NPs. These findings are signified that the strong attachment of Fe_3O_4 NPs to the nanosheet edges[28,40]. The effect of solution pH on the surface charges of PEI-*h*-BNNSs, Fe_3O_4 NPs and PEI-*h*-BNNSs@Fe_3O_4 NPs was examined by zeta potential measurements. As indicated in Fig. 3g, the zero-point charge (pH_{zpc}) values were found to be 9.3, 6.8 and 8.1 for the PEI-*h*-BNNSs, Fe_3O_4 NPs and PEI-*h*-BNNSs@Fe_3O_4 NPs, respectively[28,40,42]. The great pH_{zpc} value of PEI-*h*-BNNSs originates from the high content of amino (−N, − NH, and $-NH_2$) residues on their surfaces[28,34,35,40–43]. Besides, the pH_{zpc} value of the PEI-*h*-BNNSs@Fe_3O_4 NPs falls between those of the Fe_3O_4 NPs and PEI-*h*-BNNSs, confirming the conjugation of Fe_3O_4 NPs onto the PEI-*h*-BNNS surface edges[28,40–43]. The above-discussed results demonstrate that the surface charges of PEI-*h*-BNNSs@Fe_3O_4 NPs can be tuned by adjusting their solution pH. As indicated in Supplementary Fig. 2, the saturation magnetization values of Fe_3O_4 NPs and the proposed PEI-*h*-BNNSs@Fe_3O_4 NPs were estimated to be 120 and 74.6 emu g^{-1}, respectively[40–42]. The difference in the magnetization between the two nanomaterials mentioned above arises from the non-magnetic of PEI-*h*-BNNSs in the PEI-*h*-BNNSs@Fe_3O_4 NPs. Additionally, these two nanomaterials exhibit zero coercivity and remanence without the hysteresis loop, reflecting their super-paramagnetic behavior. In other words, the proposed PEI-*h*-BNNSs@Fe_3O_4 NPs can be collected by applying an external magnetic field at ambient temperature[42].

As examined by Fourier-transform infrared spectroscopy (FT-IR), the PEI-*h*-BNNSs@Fe_3O_4 NPs displayed apparent FT-IR peaks at 808, 1105, 1377 cm^{-1} associated with out-of-plane bending vibration of B–N–B bond, symmetric stretching vibration of B–O bond, and in-plane stretching vibration of B–N bond as indicated in Supplementary Fig. 3a [44,45]. In contrast to FT-IR spectra of *h*-BN whiskers and PEI-*h*-BNNSs (Supplementary Fig. 3b, c), a slight shift in the boron-related FT-IR peak positions from PEI-*h*-BNNSs@Fe_3O_4 NPs which signifies that, the strong interaction between *h*-BNNSs with PEI polymers and Fe_3O_4 NPs. Furthermore, the additional vibrational modes of N–H (3383 and 1657 cm^{-1}), $-CH_2$ (2956 and 2827 cm^{-1}), and Fe−O (572 cm^{-1}) reflects the successful modification of PEI polymers and Fe_3O_4 NPs on the *h*-BNNS surface[28,40,41,46].

The successful synthesis of PEI-*h*-BNNSs@Fe_3O_4 NPs encourages us to fabricate the MHAs through their freeze-drying process (Fig. 1). The as-made PEI-*h*-BNNSs@Fe_3O_4 NPs could exhibit hydroxyl and amine groups to form hydrogen bonding with hydroxyl groups from polyvinyl alcohol (PVA), which is intensively used to fabricate aerogels through the freeze-drying process[47–50].

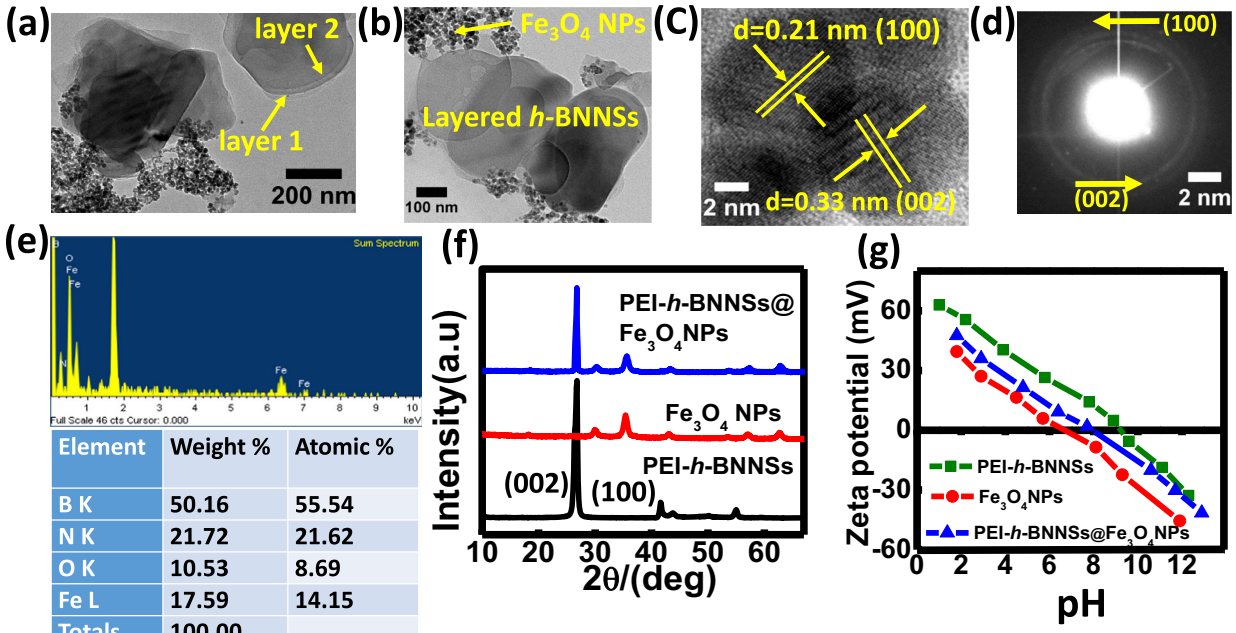

Element	Weight %	Atomic %
B K	50.16	55.54
N K	21.72	21.62
O K	10.53	8.69
Fe L	17.59	14.15
Totals	100.00	

Fig. 3 Electron microscopic techniques, diffraction pattern and surface charge of the adsorbents. Characterization of the PEI-*h*-BNNSs@Fe_3O_4 NPs: **a**, **b** Low-magnification of TEM images, **c** high-resolution of TEM image, **d** SAED pattern, **e** EDS spectra/elemental composition, **f** XRD spectra (blue line), and **g** pH-dependent zeta potential (blue line). The black and red lines in (**f**) correspond to the XRD spectra of PEI-*h*-BNNSs and Fe_3O_4 NPs, respectively. The green and red lines in (**g**) represent the pH-dependent zeta potentials of PEI-*h*-BNNSs and Fe_3O_4 NPs, respectively.

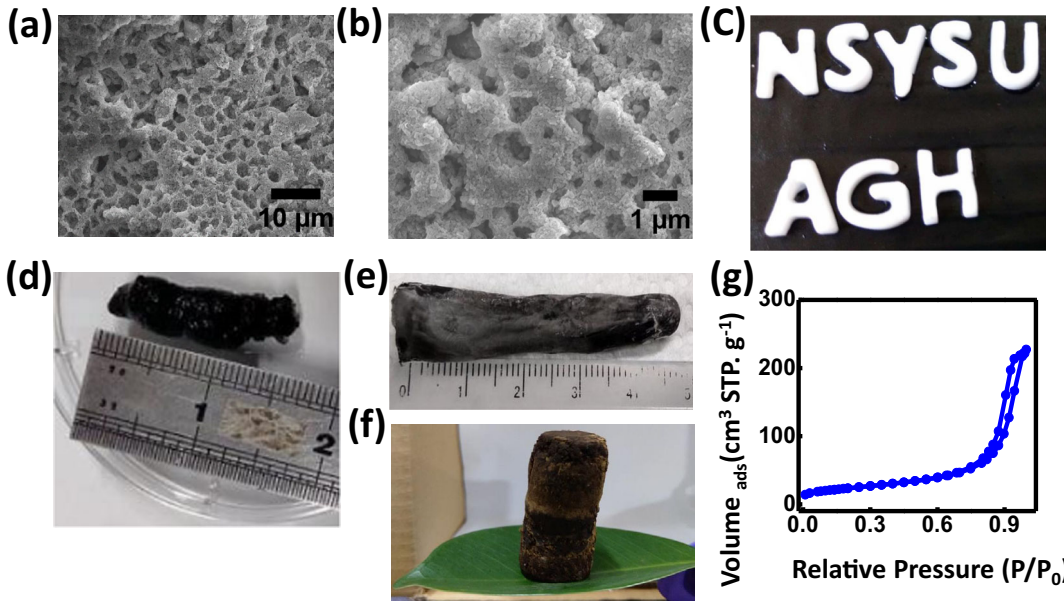

Fig. 4 Adsorbent porosity behaviors. Characterization of the *h*-BN-related aerogels. **a**, **b** SEM images of the MHAs. Photographs of (**c**) the PEI-*h*-BNNSs-loaded PVA aerogels with a shape of "NSYSU" and "AGH", (**d**) the Fe_3O_4 NP-loaded PVA aerogel (25 mg mL^{-1}), (**e**) the MHAs with a volume of (30 mg mL^{-1}), and (**f**) the MHAs with a volume of (45 mg mL^{-1}) standing on a leaf. **g** BET adsorption isotherm of the MHAs.

Therefore, the PEI-*h*-BNNSs@Fe_3O_4 NPs were blended with a PVA solution to obtain PVA hydrogels. The resultant homogenous mixture was freeze-dried to remove water molecules from PVA frameworks, producing a porous structure of the MHA. The scanning electron microscopy (SEM) images show the polygonal porous structure of MHAs with a pore size ranging from 1.0 to 10 μm (Fig. 4a, b). The formation of this porous structure could be correlated with random assembly of the PEI-*h*-BNNSs@Fe_3O_4 NPs and PVA. As depicted in Fig. 4c–e show digital photographs of the PEI-*h*-BNNSs, Fe_3O_4 NPs and PEI-*h*-BNNSs@Fe_3O_4 NPs-loaded PVA aerogels, in sequence. Intuitively, the decoration of PEI-*h*-BNNSs with Fe_3O_4 NPs caused a color change from white to black. Compared to the Fe_3O_4 NPs-loaded PVA aerogels, the porous structure of MHAs (i.e., PEI-*h*-BNNS@Fe_3O_4 NP-loaded PVA aerogels) is relatively rigid and compact. Moreover, the MHAs were capable of standing on a leaf, demonstrating their ultralight

and low-density behavior (Fig. 4f). The proposed MHAs adsorption ability and magnetic properties were separately determined by Brunauer-Emmet-Teller (BET) analysis and superconducting quantum interference device (SQUID) magnetometry. As indicated in Fig. 4g, the BET curve of MHAs belonged to a type-IV isotherm, indicating their well-formed mesoporous mature. The presence of a narrow H3-type hysteresis loop reflects that the measured materials could include slit-shaped pores on account of the assembly of nanosheets[51].

The BET surface area, pore volume and pore diameter of the present MHAs were determined to be 104.6 $m^2\ g^{-1}$ 0.13 $cm^3\ g^{-1}$ and 16.4 nm (Supplementary Fig. 4) which fall between of *h*-BN whiskers and Fe_3O_4 NPs-loaded PVA aerogels (Supplementary Table 1). The existence of long PEI chains and Fe_3O_4 NPs could distort π-π stacking interaction between two adjacent *h*-BN layers, inducing a reduction in the porosity of MHAs relative to the *h*-BN whiskers-loaded PVA aerogels[26,28,32,34,35,47,48]. In short, we reason that the mesoporous behavior could act as an efficient and reusable adsorbent due to their three-dimensional mesoporous structure, an enlarged surface area, diverse functional groups and good super-paramagnetic behavior.

Adsorption of Cr(VI) and As(V) by the MHAs

Hexavalent chromium [Cr(VI)] is intensively used in the tannery, textile and steel fabrication[1–3,13,26], while arsenic, existing as arsenite [As(III)], and arsenate [As(V)], discharge into different environmental surroundings via geothermal process and mineral deposits[28]. The maximum permissible concentrations of arsenic and chromium by the World Health Organization (WHO) are 10 and 50 ppb in drinking water[1–3,13]. According to their toxicity to human health and aquatic organisms, Cr(VI) and As(V) were selected as example contaminates to test their sorption capability of the as-proposed MHAs. As indicated in Fig. 5a, the maximum adsorption values (more than 95%) of Cr(VI) and As(V) by the MHAs were observed at pH 7.0. Considering that the PEI-*h*-BNNSs@Fe_3O_4 NPs possess the pH_{zpc} value at 8.1, the MHAs possess the positive charge due to the pronated amino groups (R-NH_3^+) of the PEI chains and also pronated surface hydroxyl groups (Fe–OH_2^+) from Fe_3O_4 NPs at pH 7.0. Therefore, these protonated amino and hydroxyl residues enable the adsorbent of (MHAs) could electrostatically interact with negatively charged CrO_4^{2-}, $HCrO_4^-$, $H_2AsO_4^-$, and $HAsO_4^{2-}$ at pH 7.0. It is noted that the charge of chemical species Cr(VI) and As(V) gradually increased with raising their solution pH[13,28,40–43]. Besides, the surface of MHAs which contains abundant hydroxyl groups (given by PVA polymers), which are highly capable of forming hydrogen bonds with CrO_4^{2-}, $HCrO_4^-$, $H_2AsO_4^-$, and $HAsO_4^{2-}$ at pH 7.0. Taken collectively, the combination of hydrogen bonding and electrostatic attraction could maximize their adsorption of Cr(VI) and As(V) on the MHA surface at pH 7.0. Interestingly, at pH extremely low and high pH, the MHAs still offered >65% uptake of Cr(VI) and As(V) from an aqueous solution. This finding implies that the electrostatic attraction of MHAs with Cr(VI) and As(V) is the critical factor influencing their absorption capability. For example, at pH 9.0, strong electrostatic repulsion is expected to exist between the MHAs and $HAsO_4^{2-}$. However, the MHAs adsorption of As(V) still kept approximately 96%. Therefore, we recommend that hydrogen bonding is the predominant driving force to trigger the MHAs to interact with Cr(VI) and As(V) in an aqueous solution. In support of the above-mentioned discussion, the adsorption isotherm experiments were conducted to determine their adsorption enthalpy of Cr(VI) and As(V) on the MHAs. The equilibrium adsorption capacity (q_e) values of Cr(VI) and As(V) on the MHAs were gradually decreased with raising the incubation temperature at pH 7.0 and 9.0 (Supplementary Fig. 5a, b), reflecting that these adsorption process are exothermic. This phenomenon was suggested to be strong electrostatic repulsion between the MHAs

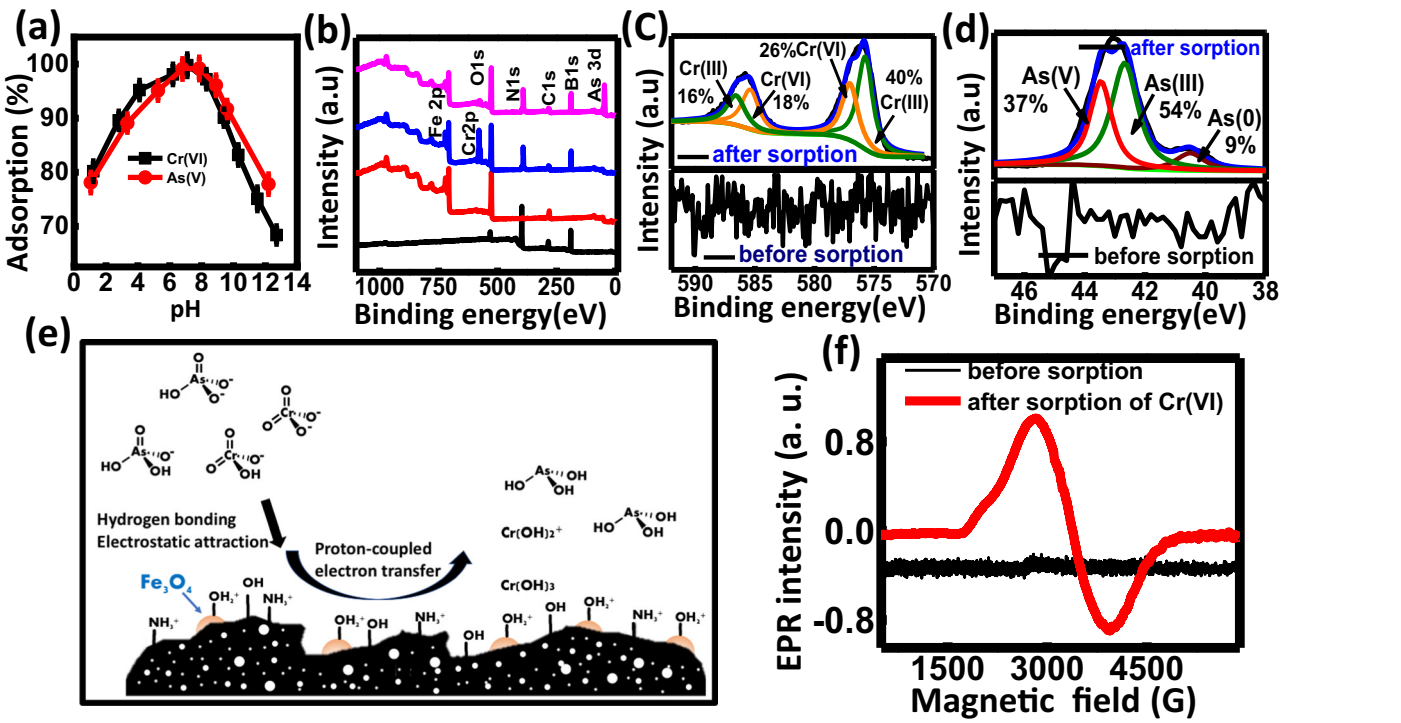

Fig. 5 High valued spectroscopic investigations. Examination of Cr(VI)- and As(V)-adsorbed MHAs. **a** Effect of solution pH against adsorption of Cr(VI) and As(V) on the adsorbent. **b** XPS survey spectra of PEI-*h*-BNNSs-loaded PVA aerogels (black curve), MHAs (red curve), Cr(VI)-adsorbed MHAs (blue curve) and As(V)-adsorbed MHAs (magenta curve). High-resolution XPS spectra of MHAs in the (**c**) Cr2p and (**d**) As3d regions. **e** Schematic illustration of the proposed mechanism related to the MHA's-mediated reduction of Cr(VI) and As(V). **f** EPR spectra of MHA's before and after sorption of Cr(VI) for 8 days.

and $HAsO_4^{2-}$ (or $HCrO_4^-$) at pH 9.0. Furthermore, the enthalpy changes (ΔH^0) was determined mechanism associated with binding type of MHAs to Cr(VI) and As(V). It is well documented that the London-van der Waals interaction energy is 4 to 8 kJ mol^{-1}, while the strength of hydrogen bonds varies from 8 to 40 kJ mol^{-1}.

By contrast, the enthalpy of chemisorption falls within the range of 40 to 400 kJ mol^{-1}. From Supplementary Fig. 5c and Supplementary Table 2 show that the calculated ΔH^0 values were determined in the range of −65 to −40 kJ mol^{-1} for the as developed adsorbent of MHA were mediated capturing of Cr(VI) and As(V) at pH 7.0 and 9.0. This finding are suggests that the strength of their interaction between MHAs and Cr(VI)/As(V) is close to that of hydrogen bonding, confirming that hydrogen bonding is a predominant factor for the interaction of MHAs with Cr(VI) and As(V).

The binding of Cr(VI) and As(V) to the surface of MHAs at pH 7.0 was investigated by FT-IR and X-ray photoelectron spectroscopy (XPS)[42,43,52–54]. To capture Cr(VI) and As(V) by MHAs led to the formation of peak position at 904 and 997 cm^{-1}, which are the characteristic of Cr–O stretching vibration in $HCrO_4^-$ (Supplementary Fig. 6a)[42,43] and the As–O stretching vibration in $H_2AsO_4^-$ (Supplementary Fig. 6b)[53–55], respectively. In contrast to, XPS survey spectra of the PEI-*h*-BNNSs-loaded PVA aerogels (black curve in Fig. 5b) and MHAs (red curve in Fig. 5b), the additional peaks are corresponding to Cr(VI) and As(V) appeared in the XPS measurements of Cr(VI)- and As(V)-adsorbed MHAs, respectively (blue and magenta curves in Fig. 5b). In more detail, the adsorption of Cr(VI) by MHAs generated two peaks position at 575.9 and 585.6 eV, which are the characteristic binding energy of $Cr2p_{3/2}$ and $Cr2p_{1/2}$, respectively (Fig. 5c). Deconvolution of the $Cr2p_{1/2}$ peak results in two gaussian bands at 586.4 and 584,9 eV, which are assigned to be Cr(III) and Cr(VI) oxidation states, respectively[42,43]. Likewise, the Cr $2p_{3/2}$ peak can be divided into two gaussian bands at 575.4 and 577.2 eV, which are separately identified to the Cr(III) and Cr(VI) oxidation states. Although the reduction of Cr(VI) to Cr(III) proceeds easier at lower pH[56], the electron-rich functional groups (i.e., $–NH_2$ and –OH) of the MHAs and Fe(II) ions from Fe_3O_4 NPs still triggering the reduction of the adsorbed Cr(VI) to Cr(III) at pH 7.0[57]. Also, the proton-coupled electron transfer, occurring from protonated amine (from PEI) and hydroxyl groups (from Fe_3O_4 NPs, MHA) the adsorbed Cr(VI), is beneficial for the reduction of Cr(VI). Similarly, Ding et al. found that protonated imine groups from polyaniline composites could serve as a proton-coupled electron donor to convert the adsorbed Cr(VI) to Cr(III)[56]. Besides, the oxidation state of Fe in the MHAs before and after the adsorption of Cr(VI) was studied by XPS (Supplementary Fig. 7). In contrast, the $Fe2p_{3/2}$ and $Fe2p_{1/2}$ peaks were identified that before and after sorption of Cr(VI) on to the surface of adsorbent besides, there is slight shifting to higher binding energies. Considering that, atoms with higher positive oxidation states are exhibits higher binding energies in the XPS spectrum, the adsorption of Cr(VI) on the adsorbent surface caused an increased ratio of Fe(III) to Fe(II). In other words, the reaction with Cr(VI) and MHAs facilitates the electron transfer from Fe(II) to Cr(VI), resulting in the formation of Fe(III) and Cr(III)[58]. In the high-resolution XPS spectra from after sorption of arsenic in the As 3d region (Fig. 5d), further de-convoluted into three more peaks positions at 43.7, 42.6 and 40.3 eV which are identified to be As(V), As(III) and As(0) oxidation states, respectively. It's suggested that, the adsorbed As(V) on the surface of adsorbent (MHAs) undergoes the same reduction process as follows on Cr(VI). The above-discussed mechanism are associating with MHAs mediated reduction of Cr(VI) and As(V) as illustrated in Fig. 5e. In order to support, those above-discussed results the oxidation states of Cr(VI) bounded with surface of adsorbent (MHAs) after 8 days were determined by electron paramagnetic resonance (EPR). A comparison in the EPR spectra before and after sorption of Cr(VI) on the surface of adsorbent which reveals that, a broad EPR peak position an identified g value of approximately 2.00 (Fig. 5f), which are confirming that, the appearance of Cr(III) on the adsorbent surface[59,60]. It's worth to mentioning that Cr(V) exhibits a sharp peak in the EPR measurement[59,60], while no EPR peak was detectable in the analysis of Cr(VI) due to paired electrons[61]. The difference in the EPR signal profile between Cr(III) and Cr(V) reflects that, the proposed adsorbent can trigger the reduction from Cr(VI) to Cr(III) rather than Cr(V). In short, under neutral pH condition, the MHA-mediated removal of Cr(VI) and As(V) which mainly involves the following processes: (i) Cr(VI) and As(V) species are adsorbed on the surface of adsorbent through their combination of hydrogen bonding and electrostatic interactions; (ii) the redox reactions are favors due to electron transferring from the functional groups on the surface of adsorbent [i.e., $–NH_2$, –OH, Fe(II)], and the adsorbed anionic species from Cr(VI)/As(V); (iii) the adsorbed Cr(VI)/As(V) were partially converted into corresponding to their reduced form of Cr(III) and As(III)/As(0), respectively; the relevant reactions were described in the following chemical equations:

$$HCrO_4^- + 3Fe^{2+} + 7H^+ \rightarrow Cr^{3+} + 3Fe^{3+} + 4H_2O \quad (1)$$

$$CrO_4^{2-} + 3Fe^{2+} + 8H^+ \rightarrow Cr^{3+} + 3Fe^{3+} + 4H_2O \quad (2)$$

$$H_2AsO_4^- + 5Fe^{2+} + 6H^+ \rightarrow As^0 + 5Fe^{3+} + 4H_2O \quad (3)$$

$$HAsO_4^{2-} + 5Fe^{2+} + 7H^+ \rightarrow As^0 + 5Fe^{3+} + 4H_2O \quad (4)$$

$$H_2AsO_4^- + 2Fe^{2+} + 3H^+ \rightarrow H_3AsO_3 + 2Fe^{3+} + H_2O \quad (5)$$

$$HAsO_4^{2-} + 2Fe^{2+} + 4H^+ \rightarrow H_3AsO_3 + 2Fe^{3+} + H_2O \quad (6)$$

(iv) the resultant Cr(III) could not only precipitate as $Cr(OH)_3$ at neutral pH but also react with Fe(III) to form Fe(III)–Cr(III) oxyhydroxides; the formation of As(0) and H_3AsO_3 may directly deposits on their surface of adsorbent (MHAs)[58]. The adsorption of kinetics and isotherms were well documented to understand their adsorption mechanism of Cr(VI)/As(V) on the proposed adsorbents which are including PEI-*h*-BNNSs-loaded PVA aerogels, Fe_3O_4 NPs-loaded PVA aerogels and MHAs. Moreover, the maximum adsorption capacity (q_{max}) of the three different kind of adsorbents for Cr(VI) and As(V) was estimated by analyzing the adsorption isotherm-related modeling. As shown Fig. 6a, b the time-dependent adsorption kinetic curves of Cr(VI) and As(V) by the three type of aerogels at pH 7.0. In comparison to the PEI-*h*-BNNSs and Fe_3O_4 NPs-loaded PVA aerogels, the MHAs provided a relatively rapid and high uptake of Cr(VI) and As(V) from an aqueous solution. Moreover, the adsorption kinetics data mentioned above were analyzed by two typical kinetic models. The fitting curves indicate that the pseudo-second-order kinetic model has a larger correlation coefficient than the pseudo-first-order kinetic model in all three proposed aerogels (Fig. 6a, b; Supplementary Table 3). In other words, the adsorption of Cr(VI) and As(V) on the proposed aerogels mainly relies on chemisorption process[42,43,62]. The adsorption isotherm was constructed by plotting their equilibrium concentration (C_e) of Cr(VI) in solution against the equilibrium adsorption capacity (q_e) of Cr(VI) on a fixed amount of the proposed aerogels (Fig. 6c); the adsorption isotherm for As(V) was also created in the same way (Fig. 6d). As a result, each type of aerogels displayed in L-type of adsorption for sorption of Cr(VI) and As(V)[63], which are well-fitted with Freundlich isotherm model ($R^2 > 0.98$; Supplementary Table 4) as below:

$$q_e = K_F C_e^{1/n} \quad (7)$$

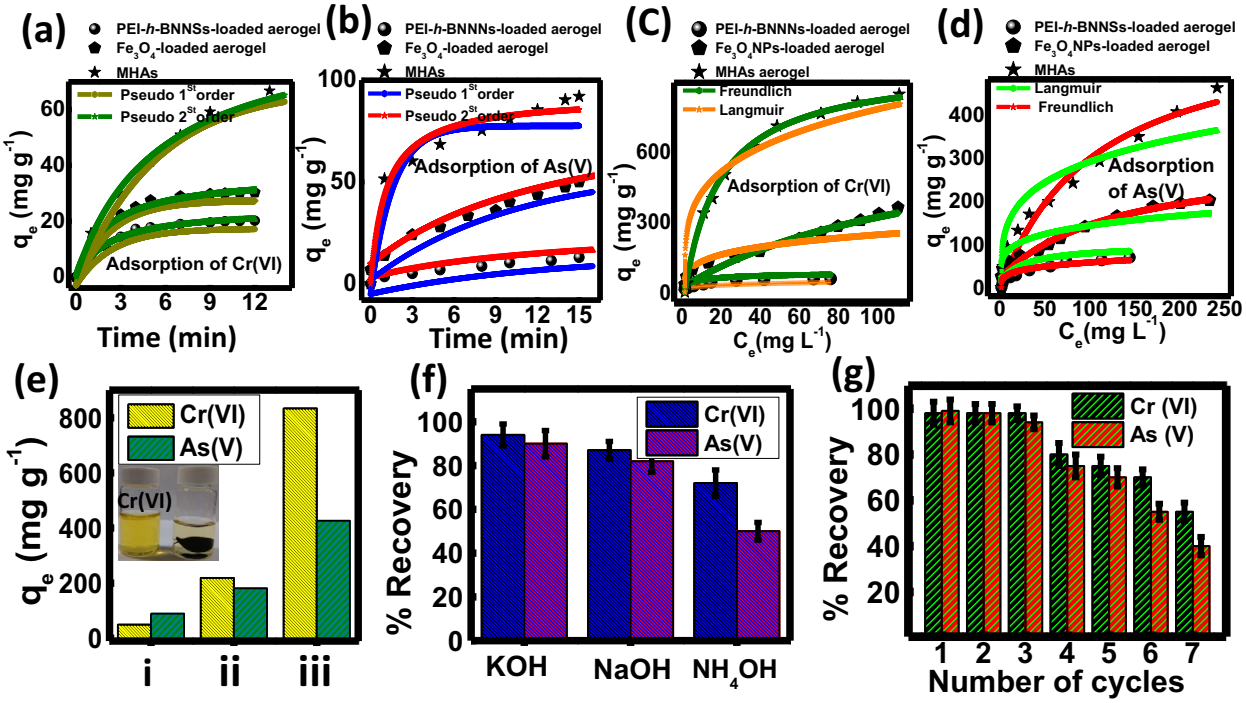

Fig. 6 Modeling studies on heavy metals sorption of isotherm, kinetics and regeneration of adsorbent. Aerogel-mediated removal of Cr(VI) and As(V). Kinetic adsorption curves of the PEI-*h*-BNNSs-loaded PVA aerogels, Fe_3O_4 NPs-loaded PVA aerogels, and MHAs for (**a**) Cr(VI) and (**b**) As(V). Modeling of adsorption curves with the pseudo-first-order kinetics (**a**: dark yellow curve; **b**: dark blue curve) and pseudo-second-order kinetic (**a**: dark green curve; **b**: red curve). Adsorption isotherms of the PEI-*h*-BNNSs-loaded PVA aerogels, Fe_3O_4 NPs-loaded PVA aerogels, and MHAs for (**c**) Cr(VI) and (**d**) As(V). Adsorption isotherms modeling Fitting with the Freundlich model (**c**: dark green curve; **d**: red curve) and Langmuir model (**c**: dark orange curve; **d**: fluorescent green curve). **e** The q_{max} values of Cr(VI) and As(V) on the surface of adsorbents are (i) PEI-*h*-BNNSs-loaded PVA aerogels, (ii) Fe_3O_4 NPs-loaded PVA aerogels and (iii) MHAs. **f** The recovery of Cr(VI) and As(V) obtained from the elution of Cr(V) and As(V)-desorbed from MHAs with 0.1 M of KOH, NaOH, and NH_4OH. **g** The reusability of MHAs for capturing and liberating of Cr(VI) or As(V). **a**–**g** The aerogels (2.0 g) were incubated with 10−600 mg mL^{-1} of Cr(VI) or As(V) at pH 7.0 and 298 K for (**a**, **b**, **c**–**g**) 0−15 min.

where K_F and n values are Freundlich constant and adsorption intensity, respectively. This result reflects that, their surface of the proposed aerogels exhibits different types of binding sites (i.e., heterogeneous surface) for multilayer adsorption of Cr (VI) and As(V). Moreover, the obtained n values of the proposed aerogels for capturing Cr(VI) and As(V) are larger than 1.0 (Supplementary Table 4), signifying their favorability of Cr(VI) and As(V) adsorption. We further determined their q_{max} values according to the following Halsey equation:

$$K_F = \frac{q_{max}}{C_0^{1/n}} \quad (8)$$

The q_{max} values of Cr(VI) and As(V) on the MHAs were respectively, 833 and 426 mg g^{-1}, which are remarkably higher than the PEI-*h*-BNNSs-loaded PVA aerogels, Fe_3O_4 NPs-loaded PVA aerogels, and other reported adsorbents (Fig. 6e; Supplementary Tables 5 and 6).

The reusability experiments were also examined to determine their sustainability of the proposed MHAs. To keep this consideration, non-hazardous solutions which are including KOH, NaOH and NH_4OH were selected to elute the adsorbed Cr(VI) and As(V) during the adsorption-desorption cycles. Figure 6f shows that KOH provided better efficiency for eluting the deposited Cr(VI)/As(V) from the MHAs as compare than NaOH and NH_4OH. This phenomenon can be elucidated as follows: Since KOH and NaOH are fully dissociated, the produced OH^- ions are efficiently competing with the adsorbed anionic species from Cr(VI)/As(V) for the surface of binding sites (MHA). To considering that, the hydrated radius of K(I) is smaller than that of Na(I), however K(I) ions can pass through the porous structure more efficiently as a result more opportunities to form their corresponding their eluting salt (e.g., K_2CrO_4). After the desorption of Cr(VI) and As(V), the MHAs were rinsed numerous times with a neutral buffer to activate their binding sites. Recycling studies display that the MHAs maintained approximately 60% uptake of Cr(VI)/As(V) in the sixth and fourth cycles of adsorption, respectively (Fig. 6g). However, the adsorption capacity of the MHAs dropped down to about 40% in the seventh cycle of adsorption, reflecting that the irreversible adsorption of Cr(VI) and As(V) still occur during the successive adsorption-desorption cycles. Due to their advantages of large adsorption capacity, good reusability, multiple heterogeneous binding sites and fast adsorption rate, we further exploited the MHAs to clean up chromium- and arsenic-contaminated soil-sludge water samples. These samples were collected from Erren River in Tainan, Art Museum in Kaohsiung, and Love River in Kaohsiung. The collected soil-sludge water samples were digested with concentrated by HNO_3 and HF in a microwave system. Inductively coupled plasma mass spectrometry (ICP-MS) was used to quantify their concentrations of total chromium and arsenic in the digested soil-sludge water samples. Besides, the MHAs were incubated with the digested soil-sludge water samples at neutral pH for 15 mins. After collecting the MHAs by applying a magnetic field, the concentrations of total chromium and arsenic were determined by ICP-MS. As shown in Supplementary Table 7, the MHAs treatment were triggered >95% of total chromium and arsenic were removed from three different kind of soil-sludge samples. Accordingly, the MHAs can be a promising adsorbing material to remove toxic chromium and arsenic from complex sludge water samples.

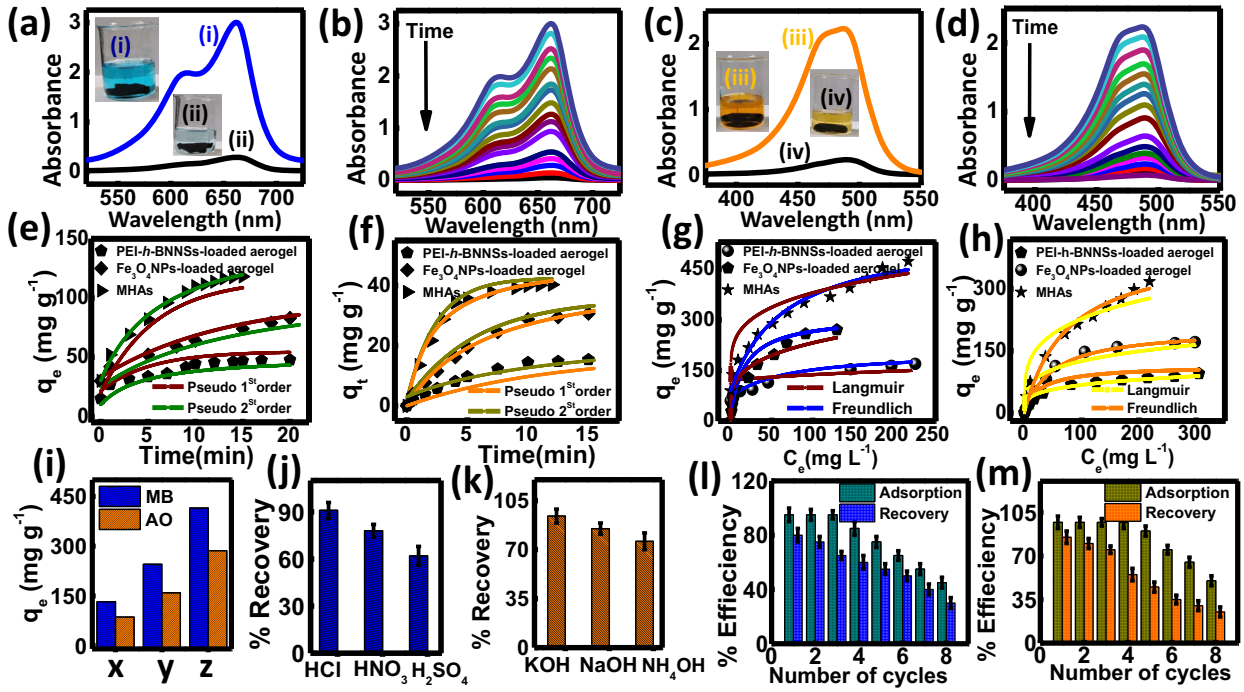

Fig. 7 Modeling studies on organic dyes sorption of isotherm, kinetics and regeneration of adsorbent. Aerogel-mediated removal of MB and AO. Absorption spectra and photographs of (**a**) 50 mg mL^{-1} of MB and (**c**) 50 mg mL^{-1} of AO **(i, iii)** before and **(ii, iv)** after addition of MHA's (2.0 g). Time-dependent absorption spectra of (**b**) 50 mg mL^{-1} of MB, and (**d**) 50 mg mL^{-1} of AO in the presence of MHAs (2.0 g). Kinetic adsorption curves of PEI-*h*-BNNSs-loaded PVA aerogels, Fe_3O_4 NPs-loaded PVA aerogels, and MHA's for (**e**) MB and (**f**) AO. Modeling of adsorption curves with the pseudo-first-order kinetics (**e**: brown curve; **f**: dark orange curve) and pseudo-second-order kinetic (**e**: dark green curve; **f**: dark yellow curve). Adsorption isotherms of the PEI-*h*-BNNSs-loaded PVA aerogels, Fe_3O_4 NPs-loaded PVA aerogels, and MHAs for (**g**) MB and (**h**) AO. Adsorption isotherms fitting of Langmuir model (**g**: brown curve; **h**: bright yellow curve) and Freundlich model (**g**: blue curve; **h**: dark orange curve). **(i)** The q_{max} values of MB and AO on the surface of (x) PEI-*h*-BNNSs-loaded PVA aerogels, (y) Fe_3O_4 NPs-loaded PVA aerogels, and (z) MHAs. **j** The recovery of MB obtained from multiple washing of MB-adsorbed MHA's with three elution solutions. **k** The recovery of AO obtained from the washing of MHA's with three elution solutions. **l**, **m** The reusability of MHAs for capturing and liberating their **(l)** MB and (m) AO. **e**–**m** The aerogels (2.0 g) were incubated with 10−500 mg mL^{-1} of MB at pH 8.5 or AO at pH 4.5 for (**e**) 0−20 min and (**f**–**m**) 0–15 min at 298 K.

Adsorption of MB and AO by the MHAs

Dyes originate from industrial activities such as textile, cosmetics, leather, food, pharmaceutical, paper productions (pulp), paint and varnish[2,4,9]. Effluents discharged from dyeing industries are carcinogenic, mutagenic and more toxic to humans and ecological organisms[21–25]. Since the surface charge of MHAs can be either positive or negative by adjusting solution pH, we reason that the MHAs could electrostatically interact with cationic dyes at high pH and anionic dyes at lowering pH[2,4,9,21–25,64]. Cationic MB and anionic AO were chosen to examine the adsorption capacity of the proposed adsorbents are PEI-*h*-BNNSs-loaded PVA aerogels, Fe_3O_4 NPs-loaded PVA aerogels and MHAs. The proposed MHAs were separately incubated with MB at pH 8.5 and AO at pH 4.5 for 30 min, we observed a remarkable reduction in the absorption intensity of MB and AO (Fig. 7a, c) and a visible color change in MB and AO solutions (inset in Fig. 7a, c[2,24,25,64]. An increase in the contact time of the MHAs with MB and AO led to a progressive reduction in their adsorption intensity (Fig. 7b, d). Evidently, the MHAs captured 90% of MB and AO molecules from an aqueous solution within 30 min of contact time. The adsorption kinetics and isotherm data are associated with MHAs for adsorption of MB and AO were well-correlated through pseudo-second-order kinetic model and Freundlich model (Fig. 7e–h; Supplementary Tables 3 and 4). It is recommended that the MHAs exhibit the heterogeneous surface for multiple-layer chemisorption of MB and AO. We also discovered the same adsorption behavior for MB and AO in the case of the PEI-*h*-BNNSs- and Fe_3O_4 NPs-loaded PVA aerogels (Fig. 7–h; Supplementary Tables 3 and 4). The q_{max} values of MHAs for capturing MB and AO were determined to be 415 and 286 mg g^{-1}, which is superior to those obtained from the PEI-*h*-BNNSs-loaded PVA aerogels, Fe_3O_4 NPs-loaded PVA aerogels, and BN-related materials and also other previously reported adsorbents (Fig. 7i; Supplementary Tables 8 and 9). The reusability of MHAs involves the liberation of adsorbed MB and AO molecules from the surface of adsorbent and the regeneration feasibilities of surface binding sites for capturing another subsequent cycles from MB and AO molecules. Therefore, we reason that the MB-attached MHAs should be treated with a strong acid, triggering to the protonation of their surface functional groups are amino and hydroxyl. As a result, the MHAs have enough positive charges to repel the adsorbed MB molecule, resulting in their liberation into an aqueous solution[24,25,64]. Figure 7j represents that more than 90% of the bound MB molecules on the MHA surface were eluted with 0.1 M HCl, confirming our hypothesis. However, with H_2SO_4 reflux, the carbonization of the adsorbed MB molecules could reduce their desorption efficiency. Besides, HNO_3 could oxidize the MHA surface during the elution process, interfering with the-desorption of MB. On the other hand, we hypothesize that the AO-adsorbed MHAs should be incubated with a strong base, activating the dissociation of their surface hydroxyl groups. Therefore, electrostatic repulsion between AO molecules and the MHAs can liberate the bound ones. As shown in Fig. 7k, 0.1 M KOH triggered more efficient desorption of AO from the MHA surface than 0.1 M NaOH and NH_4OH. The explanations are associated

with KOH-mediated elution of the bound Cr(VI) and As(V) can be applied here also to interpret the similar phenomenon were mentioned above. As depicted in Fig. 7l, m, the MHAs still efficiently capture for more than 90% of MB and AO molecules during three and four successive adsorption-desorption cycles, respectively[65–67]. However, after six and four sequential adsorption-desorption cycles, the low recoveries (<50%) of MB and AO could arise from the irreversible adsorption of adsorbates and elution solution-mediated conversion of adsorbates[65–67]. According to the above findings, we point out that, the MHAs not only exhibit an excellent adsorption capacity to capturing the MB and AO and also shows good reusability performance.

Adsorption of thermodynamics

The thermodynamic studies were conducted to ascertain feasibility of the aerogels as an adsorbent for capturing of Cr(VI), As(V), MB and AO. The thermodynamic parameters of the standard Gibbs free energy (ΔG^0), standard enthalpy (ΔH^0) and standard entropy (ΔS^0) were determined by the Gibbs–Helmholtz and Van't Hoff equations as below:

$$\Delta G^0 = -RT\ \ln K \tag{9}$$

$$\ln \mathrm{K} = \frac{-\Delta H^0}{RT} + \frac{\Delta S^0}{R} \tag{10}$$

where R is the gas constant (8.314 J K $^{-1}$ mol $^{-1}$), T is the absolute temperature (Kelvin) and the equilibrium constant K was obtained from the ratio of solid phase uptake in different pollutants from Cr(VI), As(V), MB and AO concentration at equilibrium (mg L^{-1}) to the concentration in aqueous solution (mg L^{-1}). From Supplementary Fig. 8 shows that thermodynamic curves of the three proposed adsorbents were established by plotting ln K versus 1/T; the resultant slope and intercept of Van't Hoff plots correspond to ΔH^0 and ΔS^0 values of the three proposed aerogels, respectively. As indicated in Supplementary Fig. 8a, the negative slopes of the plots reflect that the uptake of Cr(VI) As(V), MB and AO by the PEI-*h*-BNNSs-loaded PVA aerogels is endothermic and nonspontaneous. By contrast, the positive slopes from plots as shown in Supplementary Fig. 8b, c indicates that, adsorption process of the Fe_3O_4 NPs-loaded PVA aerogels and MHAs is exothermic and enthalpy favored. Besides, the slope from the plot for the MHAs was steeper than that to Fe_3O_4 NPs-loaded PVA aerogels, supporting that the MHAs have better maximum adsorption capacity than the other two type of aerogels. From Supplementary Table 10 collects the thermodynamic parameters values are (ΔG^0, ΔH^0, and ΔS^0) for the binding of Cr(VI) As(V), MB and AO to the surface of three proposed aerogels at various temperatures are 298, 308, 318 and 328 K. The small negative ΔG^0 values confirm the feasibility and spontaneity of the three proposed aerogels for the physical adsorption of Cr(VI), As(V), MB, and AO at a given temperature; it is noted that the ΔG^0 values of the spontaneous physical and chemisorption processes fall within the range of −20 to 0 and −80 to −400 kJ mol^{-1}, respectively[68–70]. In other words, the elution of the adsorbents from the three proposed aerogels is relatively simple without the breaking of chemical bonds. Moreover, the MHAs possessed a larger negative ΔG^0 value at a lower temperature than the PEI-*h*-BNNSs and Fe_3O_4 NPs-loaded PVA aerogels, reflecting their better adsorption capability. For the adsorption process of the PEI-*h*-BNNSs-loaded PVA aerogels, the obtained positive ΔS^0 values indicate that the adsorbates could trigger their structural changes, resulting in the liberation of adsorbed water molecules. In the case of the Fe_3O_4 NPs-loaded PVA aerogels and MHAs, the resultant negative ΔS^0 values which involve the loss of freedom of the adsorbates and no significant change in the internal structure of adsorbents. It's concluded that the adsorption mechanism of MHAs is driven by physical adsorption, which is very rapid and more spontaneous at lower temperatures.

DISCUSSION

We have demonstrated the successful synthesis of PEI-h-BNNSs via melamine and boric acid thermal poly-condensation, followed by pyrolysis, ultra-sonication treatment and PEI modification. Incorporating the co-precipitation reaction with PEI-*h*-BNNSs promotes the in-situ formation of Fe_3O_4 NPs on the nanosheet surface. The hydrogels composed of PEI-*h*-BNNSs@Fe_3O_4 NPs and PVA polymers can be fabricated into the MHAs through their freeze-drying process. The as-made MHAs serve as a powerful adsorbent to remove Cr(VI), As(V), MB and AO from an aqueous solution and their adsorption behavior which follows Freundlich isotherm model and a pseudo-second-order model. The adsorption capacity of MHAs allows the removal of >95% for Cr(VI) and As(V) in contaminated soil-sludge samples. In contrast to the PEI-*h*-BNNSs-loaded PVA aerogels, Fe_3O_4 NPs-loaded PVA aerogels and other previously reported adsorbents, the MHAs provide numerous distinct advantages, including (1) the presence of highly mesoporous structures with a large specific surface area of 104.6 m^2 g^{-1}, (2) the possession of diverse and abundant functional groups (−N, −NH, −NH_2, and −OH) on the surface, (3) outstanding adsorption capacity for capturing of Cr(VI) (833 mg g^{-1}), As(V) (426 mg g^{-1}), MB (415 mg g^{-1}) and AO (286 mg g^{-1}), (4) in-situ reduction of Cr(VI) to Cr(III) and As(V) to As(III), (5) more than three successive adsorption-desorption cycles for >80% uptake of Cr(VI), As(V), MB, and AO and (6) the accessible collection of MHAs by applying an external magnetic field. Accordingly, our research work discloses that the as-made aerogels composed of *h*-BN-based materials with PVA polymers have great potential candidate in large-scale water treatment.

METHODS

Chemicals

Melamine was bought from Alfa-Aesar (Ward Hill, MD, USA). Boric acid, PEI (M.W., 750 kDa), polyvinyl alcohol (PVA; M.W., 130,000 kDa) were obtained from Sigma-Aldrich (St Louis, MO, USA). A standard solution of chromium (VI) and arsenic (V) was acquired from Merck (1000 mg L^{-1}; Darmstadt, Germany) and then diluted to the desired concentration. MB, AO, $FeCl_2{\cdot}4H_2O$, and $FeCl_3{\cdot}6H_2O$ were purchased from Showa Chemicals (Tokyo, Japan). All other reagents were procured from analytical grade. Milli-Q ultrapure water (Milli-Pore, Hamburg, Germany) was used in all the experiments.

Synthesis of the PEI-*h*-BNNSs

5.0 g of boric acid and 3.5 g of melamine were dissolved in 300 mL of Milli-Q water. The as-obtained mixture was heated up to 85 °C for 5 h and then cooled down to ambient temperature. The resultant white precipitates were pyrolysis in a vertical tube furnace at 850 °C with a flow of N_2 atmosphere (0.5 L min^{-1}) for 10 h[1–3,31]. After cooling down to ambient temperature, the formed products (white buffy) were ground into fine particles with a pestle and mortar. Subsequently, 1.5 g of the resultant particles corresponding to the *h*-BN whiskers was dispersed in 150 mL of 5.0 M HCl. The obtained solution was treated with an ultrasonic probe sonication system (230 W; UP-100 Ultrasonic Processor, ChromTech, Taiwan) for 6 h, followed by centrifugation at 4500 rpm for 30 min. The exfoliated *h*-BNNSs in the supernatant were washed extensively with Milli-Q water until a neutral pH was reached[18]. The as-made *h*-BNNSs (45 mg mL^{-1}, 100 mL) were functionalized with PEI (10 % w/v, 20 mL) in ultrasonic bath for 2 h[32,43]. The formed solid products (milky white) were washed thoroughly with Milli-Q water to eliminate their excess PEI molecules. After discarding the supernatant from the final wash, the resultant solid products corresponding to the PEI-*h*-BNNSs were dried and stored at room temperature without light and humidity prior to use in the synthesis of MHAs.

Synthesis of the PEI-*h*-BN quantum dots

Briefly, the *h*-BN whiskers (0.25 g) was uniformly dispersed in DMF (250 mL), followed by ultra-sonication (Elmasoni E60H; Elma Schmidbauer GmbH, Singen, Germany) at 400 W and 4 °C for 24 h. Afterwards, the

resultant solution was centrifuged at 4500 rpm for 30 min. The obtained supernatant was further boiled at 130 °C for 10 h under continuously stirring and then centrifuged at 12,000 rpm for 60 min. The nanoparticles in the second supernatant were denoted as the *h*-BN quantum dots[71]. The procedure associated with the PEI-mediated modification of *h*-BN quantum dots was the same as that used in the preparation of the PEI-*h*-BNNSs[32,43].

Preparation of aerogels

(a) PEI-*h*-BNNSs-loaded PVA aerogels. A known quantities of PEI-*h*-BNNSs (0.5−1.0 g) were mixed with 3 mL of 3.0% w/w PVA aqueous solution. The resultant mixture was stirred at 80 °C for 30 min; the final concentrations of PEI-*h*-BNNSs ranged from 10.0 to 40.0 mg mL^{-1}. The suspension of PVA-modified PEI-*h*-BNNSs was filled in a rubber mold and further cooled at −70 °C by liquid nitrogen[31]. After 2 h, the frozen products were lyophilized by freeze-dryer (FD-5030, PanChum Sci. Corp, Taiwan) for 48 h (−57.2 °C and 5.9 Pa) to remove the excess surface moisture. The obtained aerogels were stored in a dry and sealed container at 25 °C. **(b) MHAs**. 0.5 g of PEI-*h*-BNNSs in Milli-Q water (100 mL) was dispersed by ultra-sonication for 20 min. The dispersed PEI-*h*-BNNSs were mixed with a solution (100 mL) containing 1.4 g of $FeCl_2{\cdot}4H_2O$ and 3.6 g of $FeCl_3{\cdot}6H_2O$ under gentle stirring. The mixture was bubbled with nitrogen gas for 30 min, followed by heating to 80 °C for 30 min. Subsequently, 10 mL of 5.0 M NH_4OH was injected rapidly into the heating solution, which was left to stir for another 60 min. After cooling down to ambient temperature, the obtained black-colored solution was washed thoroughly with Milli-Q water[42]. The as-prepared PEI-*h*-BNNSs@Fe_3O_4 NPs (30 mg mL^{-1}, 80 mL) were blended with 3 mL, 3.0% w/w of PVA for 60 min, followed by injecting 2 mL of 4.0 M H_2SO_4. The obtained mixture was kept in an autoclave at 180−200 °C for 24 h[31,47], cooled down to ambient temperature, washed thoroughly with Milli-Q water and then treated by a freeze dryer (−57.2 °C and 5.9 Pa) for 48 h. The resultant MHAs were stored in a dry environment at 25 °C. **(c) Fe_3O_4 NPs-loaded PVA aerogels**. The synthesis of bare Fe_3O_4 NPs followed by previously reported methods[28,40,42], and their detailed procedures were discussed in the Supporting Information. The as-prepared Fe_3O_4 NPs (25 mg mL^{-1}, 80 mL) were mixed with 3.0 mL of 3.0% w/w, PVA for 60 min. After introducing 2 mL of 4.0 M H_2SO_4 to the resultant mixture of solution was treated at 180−200 °C for 24 h. The obtained products were washed extensively with Milli-Q water, subsequently treated by a freeze dryer and then stored at 25 °C[47].

Mass concentration of nanomaterials

Aqueous solutions of different nanomaterials were passed through cellulose acetate syringe filters (0.22 µm), oven-dried at 80 °C, and then stored at 50% relative humidity at 25 °C for 48 h. The masses of unloaded and nanomaterial-loaded syringe filters were weighed on an electronic microbalance (MSA6.6S-0CE-DM, Sartorius, Goettingen, Germany) with the readability of 10^{-6} g. In sequence, the mass concentrations of PEI-*h*-BNNSs@Fe_3O_4 NPs, PEI-*h*-BNNSs, and Fe_3O_4 NPs were determined to be 41.3, 16.9, and 27.6 mg mL^{-1}.

Batch adsorption study

The adsorption behavior and mechanism of PEI-*h*-BNNSs-loaded PVA aerogels, Fe_3O_4 NPs-loaded PVA aerogels and MHAs were studied by various isothermal models and kinetics at 303 K. To establish the adsorption isotherm curves, we incubated the fixed amount of aerogels (2.0 g) with 10−600 mg mL^{-1} of Cr(VI) at pH 4.3−7.0 and 10−600 mg mL^{-1} of As(V) at pH 4.3−7.0 for 15 min. The aerogels in the resultant solutions were collected by magnetic separation or centrifugation. Subsequently, the concentration of Cr(VI) or As(V) in the supernatant was determined by inductively coupled plasma mass spectrometry (ICP-MS; PerkinElmer, Sciex-Elan DRC Plus; software used: Elan-6100 DRC PLUS). The collected aerogels were washed with a mild base solution [(10 mL; 0.1 M of KOH, NaOH and NH_4OH)] and then used in the next adsorption cycle. Moreover, the adsorption isotherms of MB and AO were treated by the as made aerogel by varying their initial concentration C_0 values obtained from 10 to 500 mg mL^{-1} at pH 8.5 and 4.5, respectively. After centrifugation or magnetic separation, the concentration of MB or AO in the supernatant was measured on a UV–Vis spectrometer (V-630, Jasco, Tokyo, Japan). The MB- and AO-adsorbed aerogels were rinsed with a strong acid [(10 mL; 0.1 M of HCl, HNO_3, and H_2SO_4)] and a strong base [(10 mL; 0.1 M of KOH, NaOH, and NH_4OH)], respectively. The procedure mentioned above was repeated to test their reusability of the adsorbents.

The kinetic studies were carried out by contacting different kinds of aerogels with 100 mg mL^{-1} of Cr(VI), 100 mg mL^{-1} of As(V), 50 mg mL^{-1} of MB, and 50 mg mL^{-1} of AO at pH 7.0, 7.0, 8.5 and 4,5, respectively[21,24–26,28,40,42,43]. After 0−20 min, the resultant aerogels were collected by magnetic separation. The final concentrations (C_e) of free Cr(VI), As(V), MB and AO in the supernatant were measured by ICP-MS or UV-visible absorption spectrometer. It is noted that the maximum absorption wavelengths of MB and AO were 660 and 490 nm, respectively[23–25,64]. The amounts of Cr(VI), As(V), MB and AO on the aerogels at equilibrium, q_e (mg g^{-1}), were calculated by the following equation:

$$q_e = \frac{(C_0 - C_e)V}{W} \tag{11}$$

where C_e is the liquid-phase concentration of the aerogels at equilibrium, W is the weight (g) of the dry aerogels and V is the volume (L) of the tested solution. The removal efficacy (% RE) was determined according to the equation given below:

$$\%\ \mathrm{RE} = \frac{(C_0 - C_f)}{C_0} \times 100 \tag{12}$$

MHA-mediated detoxification of Cr(VI) and As(V) in real-world samples

Industrial soil-sludge samples were collected from Erren River in Tainan, Art Museum in Kaohsiung, and Love River in Kaohsiung). The collected samples (5.0 g) was introduced into a 100 mL PTFE digestion vessel, followed by mixing with a digest solution (5.0 m of concentrated HNO_3 and 4 mL of concentrated HF). The resultant vessel was reacted at 210 °C and 800 W for 40 min, remained at 160 °C for 20 min, cooled to room temperature and then diluted with 10 mL of Milli-Q water. The resultant solution was treated with and without the proposed MHAs (2.0 g) under gentle shaking at pH 7.0. The concentration of total chromium and arsenic in the obtained solution was determined by ICP-MS.

Reporting summary

Further information on research design is available in the Nature Research Reporting Summary linked to this article.

DATA AVAILABILITY

The data that support the findings of this study are available from the corresponding author upon reasonable request.

CODE AVAILABILITY

All relevant codes are available at the supporting information or from the corresponding author on request.

Received: 23 February 2022; Accepted: 22 June 2022;
Published online: 04 July 2022

REFERENCES

1. Liu, F. et al. Template-free synthesis of oxygen-doped bundle-like porous boron nitride for highly efficient removal of heavy metals from wastewater. *ACS Sustain. Chem. Eng.* **6**, 16011–16020 (2018).
2. Liu, F., Yu, J., Ji, X. & Qian, M. Nanosheet-structured boron nitride spheres with a versatile adsorption capacity for water cleaning. *ACS Appl. Mater. Interfaces* **7**, 1824–1832 (2015).
3. Li, J. et al. Activated boron nitride as an effective adsorbent for metal ions and organic pollutants. *Sci. Rep.* **3**, 3208–3214 (2013).
4. Singh, S. et al. Decontamination of cationic dye brilliant green from the aqueous media. *Appl. Water Sci.* **12**, 61–71 (2022).
5. Gupta, H. & Gupta, B. Adsorption of polycyclic aromatic hydrocarbons on banana peel activated carbon. *Desalin. Water Treat.* **57**, 9498–9509 (2015).
6. Gupta, H. & Gupta, B. Vehicular tire as potential adsorbent for the removal of polycyclic aromatic hydrocarbons. *Polycycl. Aromat. Compd.* **38**, 354–368 (2018).
7. Gupta, H. Anthracene removal from water onto activated carbon derived from vehicular tyre. *Sep. Sci. Technol.* **53**, 613–625 (2018).

8. Gupta, H. PAH determination in effluent and sludge samples of paper industry. *Environ. Technol. Innov.* **9**, 115–121 (2018).
9. Soltani, T. & Entezari, M. H. Sono-synthesis of bismuth ferrite nanoparticles with high photo-catalytic activity in degradation of Rhodamine B under solar light irradiation. *Chem. Eng. J.* **223**, 145–154 (2013).
10. Yu, Y.-Q., Zhao, C., Liu, X.-H., Sui, M. & Meng, Y. Selective flocculation of pollutants in wastewater using pH responsive HM-alginate/chitosan complexes. *J. Environ. Chem. Eng.* **5**, 5406–5410 (2017).
11. Singh, P. & Borthakur, A. A review on biodegradation and photocatalytic degradation of organic pollutants: A bibliometric and comparative analysis. *J. Clean. Prod.* **196**, 1669–1680 (2018).
12. Bakshi, A. et al. Structure dependent water transport in membranes based on two-dimensional materials. *Ind. Eng. Chem. Res.* **60**, 10917–10959 (2021).
13. Kalidhasan, S., Santhana Krishna Kumar, A., Rajesh, V. & Rajesh, N. A preliminary spectroscopic investigation on the molecular interaction of metal–diphenylthiocarbazone complex with cellulose biopolymer and its application. *Spectrochimica Acta Part A* **79**, 1681–1687 (2011).
14. Zhang, W.-J., Yang, X.-Y. & Wang, D.-S. Complete removal of organic contaminants from hypersaline wastewater by the integrated process of powdered activated carbon adsorption and thermal fenton oxidation. *Ind. Eng. Chem. Res.* **52**, 5765–5771 (2013).
15. Thakur, K. & Kandasubramanian, B. Graphene and graphene oxide-based composites for removal of organic pollutants: A review. *J. Chem. Eng. Data.* **64**, 833–867 (2019).
16. Kalidhasan, S. et al. Microwave assisted solvent free green preparation and physicochemical characterization of surfactant-anchored cellulose and its relevance toward the effective adsorption of chromium. *J. Colloid interface Sci.* **367**, 398–408 (2012).
17. Dong, S. Y., Zheng, Q., Huang, G., Wang, X. H. & Huang, T. L. The coordination polymer $[Cu(bipy)(SO_4)]_n$ and its functionalization for selective removal of two types of organic pollutants. *Ind. Eng. Chem. Res.* **58**, 15416–15424 (2019).
18. Duan, S.-X. et al. HF-free synthesis of nanoscale metal−organic framework NMIL-100(Fe) as an efficient dye adsorbent. *ACS Sustain. Chem. Eng.* **4**, 3368–3378 (2016).
19. Karak, S. et al. Inducing disorder in order: Hierarchically porous covalent organic framework nanostructures for rapid removal of persistent organic pollutants. *J. Am. Chem. Soc.* **141**, 7572–7581 (2019).
20. Kalidhasan, S., Santhana Krishna Kumar, A., Rajesh, V. & Rajesh, N. Enhanced adsorption of hexavalent chromium arising out of an admirable interaction between a synthetic polymer and an ionic liquid. *Chem. Eng. J.* **222**, 454–463 (2013).
21. Li, Q. et al. Porous hexagonal boron nitride whiskers fabricated at low temperature for effective removal of organic pollutants from water. *Ceram. Int.* **42**, 8754–8762 (2016).
22. Chao, Y. et al. Gas-assisted exfoliation of boron nitride nanosheets enhancing adsorption performance. *Ceram. Int.* **45**, 18838–18843 (2019).
23. Liu, Z. et al. Novel multifunctional cheese-like 3D carbon-BN as a highly efficient adsorbent for water purification. *Sci. Rep.* **8**, 1104–1114 (2018).
24. Li, J. et al. Chemical activation of boron nitride fibers for improved cationic dye removal performance. *J. Mater. Chem. A* **3**, 8185–8193 (2015).
25. Lian, G. et al. Controlled fabrication of ultrathin-shell BN hollow spheres with excellent performance in hydrogen storage and wastewater treatment. *Energy Environ. Sci.* **5**, 7072–7080 (2012).
26. Karthikeyan, P., Elanchezhiyan, S. S. D., Preethi, J., Meenakshi, S. & Park, C. M. Mechanistic performance of polyaniline-substituted hexagonal boron nitride composite as a highly efficient adsorbent for the removal of phosphate, nitrate, and hexavalent chromium ions from an aqueous environment. *Appl. Surf. Sci.* **511**, 145543 (2020).
27. Li, J., Jin, P. & Tang, C. Cr(III) adsorption by fluorinated activated boron nitride: A combined experimental and theoretical investigation. *RSC Adv.* **4**, 14815–14821 (2014).
28. Bangari, R. S., Singh, A. K., Namsani, S., Singh, J. K. & Sinha, N. Magnetite coated boron nitride nanosheets for the removal of arsenic (V) from water. *ACS Appl. Mater. Interfaces* **11**, 19017–19028 (2019).
29. Pan, J.-J. & Wang, J.-Y. Boron nitride aerogels consisting of varied superstructures. *Nanoscale Adv.* **2**, 149–155 (2020).
30. Kamran, U., Rhee, K. Y. & Park, S.-J. Effect of triblock co-polymer on carbon-based boron nitride whiskers for efficient CO_2 adsorption. *Polymers* **11**, 913–928 (2019).
31. Lin, J. et al. Ultrafine porous boron nitride nanofibers synthesized via a freeze-drying and pyrolysis process and their adsorption properties. *RSC Adv.* **6**, 1253–1259 (2016).
32. Wu, Y.-Q. et al. Synergistic functionalization of *h*-BN by mechanical exfoliation and PEI chemical modification for enhancing the corrosion resistance of waterborne epoxy coating. *Prog. Org. Coatings* **142**, 105541 (2020).
33. Zhang, T.-Y. & Zhang, D. Aggregation reduction of atomic force microscopy sample preparation of reduced graphene oxide nanosheets. *J. Nanosci. Nanotechnol.* **10**, 5316–5319 (2010).
34. Lei, W. et al. Boron nitride colloidal solutions, ultralight aerogels and freestanding membranes through one-step exfoliation and functionalization. *Nat. Commun.* **6**, 8849–8856 (2015).
35. Lei, W., Portehault, D., Liu, D., Qin, S. & Chen, Y. Porous boron nitride nanosheets for effective water cleaning. *Nat. Commun.* **4**, 1777–1783 (2013).
36. Wan, W. C., Yu, S., Dong, F., Zhang, Q. & Zhou, Y. Efficient C_3N_4/graphene oxide aerogel macroscopic visible-light photo-catalyst. *J. Mater. Chem. A* **4**, 7823–7829 (2016).
37. Sajjad, M., Jadwisienczak, W. M. & Feng, P. Nanoscale structure study of boron nitride nanosheets and development of a deep-UV photo-detector. *Nanoscale* **6**, 4577–4582 (2014).
38. Gorbachev, R. V. et al. Hunting for monolayer boron nitride: Optical and Raman signatures. *Small* **7**, 465–468 (2011).
39. Ling, J. et al. Vibrational imaging and quantification of two-dimensional hexagonal boron nitride with stimulated Raman scattering. *ACS Nano* **13**, 14033–14040 (2019).
40. Bangari, R. S., Yadav, V.-K., Singh, J. K. & Sinha, N. Fe_3O_4-functionalized boron nitride nanosheets as novel adsorbents for removal of arsenic (III) from contaminated water. *ACS Omega* **5**, 10301–10314 (2020).
41. Chen, R. et al. Arsenic (V) adsorption on Fe_3O_4 nanoparticle-coated boron nitride nanotubes. *J. Colloid Interface Sci.* **359**, 261–268 (2011).
42. Santhana Krishna Kumar, A. et al. Magnetically separable nano-spherical g-C_3N_4@Fe_3O_4 as a recyclable material for chromium adsorption and visible-light-driven catalytic reduction of aromatic nitro compounds. *ACS Sustain. Chem. Eng.* **7**, 6662–6671 (2019).
43. Arputharaj, E. et al. Self-Assembly of poly(ethyleneimine)-modified g-C_3N_4 nanosheets with lysozyme fibrils for chromium detoxification. *Langmuir* **37**, 7147–7155 (2021).
44. Lee, D. G. et al. Scalable exfoliation process for highly soluble boron nitride nanoplatelets by hydroxide-assisted ball milling. *Nano Lett.* **15**, 1238–1244 (2015).
45. Fu., K. et al. Highly multifunctional and thermo-conductive performances of densely filled boron nitride nanosheets/epoxy resin bulk composites. *ACS Appl. Mater. Interfaces* **13**, 2853–2867 (2021).
46. Tan, M.-Q. et al. Immobilized bioactive agents onto polyurethane surface with heparin and phosphoryl choline group. *Macromol. Res.* **21**, 541–549 (2013).
47. Zhang, R.-Y., Wan, W.-C., Qiu, L.-J., Wang, Y.-H. & Zhou, Y. Preparation of hydrophobic polyvinyl alcohol aerogel via the surface modification of boron nitride for environmental remediation. *Appl. Surf. Sci.* **419**, 342–347 (2017).
48. Yang, W. et al. Pectin-assisted dispersion of exfoliated boron nitride nanosheets for assembled bio-composite aerogels. *Compos. Part A* **119**, 196–205 (2019).
49. Zhang, H. & Zhang, J.-H. The preparation of novel polyvinyl alcohol (PVA)-based nanoparticle/carbon nanotubes (PNP/CNTs) aerogel for solvents adsorption application. *J. Colloid Interface Sci.* **569**, 254–266 (2020).
50. Wang, Y.-T. et al. Green approach to improving the strength and flame retardancy of poly-(vinyl alcohol)/clay aerogels: Incorporating bio-based gelatin. *ACS Appl. Mater. Interfaces* **9**, 42258–42265 (2017).
51. Fan, H. et al. In-situ formation of Fe nanoparticles from FeOOH nanosheets on γ-Al_2O_3 as efficient catalysts for ammonia synthesis. *ACS Sustain. Chem. Eng.* **5**, 10900–10909 (2017).
52. Wu, J. et al. Core-shell CMNP@PDAP nanocomposites for simultaneous removal of chromium and arsenic. *Chem. Eng. J.* **349**, 481–490 (2018).
53. Zhou, C., Han, C. Y., Min, X.-Z. & Yang, T. Simultaneous adsorption of As(V) and Cr(VI) by zeolite supporting sulfide nanoscale zero-valent iron: Competitive reaction, affinity and removal mechanism. *J. Mol. Liq.* **338**, 116619 (2021).
54. Zubair, Y. O., Fuchida, S. & Tokoro, C. Insight into the mechanism of arsenic (III/V) uptake on mesoporous zero-valent iron−magnetite nanocomposites: adsorption and microscopic studies. *ACS Appl. Mater. Interfaces* **12**, 49755–49767 (2020).
55. Singh, P., Sarswat, A., Pittman, C. U., Mlsna, T. & Mohan, D. Sustainable low-concentration arsenite [As(III)] removal in single and multicomponent systems using hybrid iron oxide−biochar nanocomposite adsorbents: A mechanistic study. *ACS Omega* **5**, 2575–2593 (2020).
56. Ding, J. et al. Adsorption and reduction of Cr(VI) together with Cr(III) sequestration by polyaniline confined in pores of polystyrene beads. *Environ. Sci. Technol.* **52**, 12602–12611 (2018).
57. Pinakidou, F. et al. On the passivation mechanism of Fe_3O_4 nanoparticles during Cr(VI) removal from water: A XAFS study. *Appl. Surf. Sci.* **360**, 1080–1086 (2016).
58. Wang, X., Zhang, Y., Wang, Z.-W., Xu, C.-H. & Tratnyek, P. G. Advances in metal(loid) oxyanion removal by zerovalent iron: Kinetics, pathways, and mechanisms. *Chemosphere* **280**, 130766 (2021).
59. Saiz, P. G. et al. Chromium speciation in zirconium-based metal organic frameworks for environmental remediation. *Chem. Eur. J.* **26**, 13861–13872 (2020).

60. Huang, X.-N. et al. Formation mechanism of organo-chromium(III) complexes from bio-reduction of chromium (VI) by *Aeromonas hydrophila*. *Environ. Int.* **129**, 86–94 (2019).
61. Sun, M. et al. Redox conversion of chromium(VI) and arsenic(III) with the intermediates of chromium(V) and arsenic(IV) via AuPd/CNTs electro-catalysis in acid aqueous solution. *Environ. Sci. Technol.* **49**, 9289–9297 (2015).
62. Li, Z. et al. Ethanol introduced synthesis of ultra-stable 1T-MoS_2 for removal of Cr(VI). *J. Hazard. Mater.* **394**, 122525 (2020).
63. Keshteli, M. R., Farahbakhsh, M. & Savaghebi, G. R. Adsorption behaviour of glyphosate in some citrus garden soils of Iran. *Electron. J. Environ. Agric. Food Chem.* **10**, 1943–1951 (2011).
64. Wen, Z.-P., Zhang, Y., Cheng, G., Wang, Y.-G. & Chen, R. Simultaneous removal of As(V)/Cr(VI) and acid orange 7 (AO7) by nanosized ordered magnetic mesoporous Fe-Ce bimetal oxides: Behaviour and mechanism. *Chemosphere* **218**, 1002–1013 (2019).
65. Sheshmani, S., Ashori, A. & Hasanzadeh, S. Removal of acid orange 7 from aqueous solution using magnetic graphene/chitosan: A promising nano-adsorbent. *Int. J. Biol. Macromol.* **68**, 218–224 (2014).
66. Zaheer, Z., Bawazir, W. A. B., Al-Bukhari, S. M. & Basaleh, A. S. Adsorption, equilibrium isotherm, and thermodynamic studies to the removal of acid orange 7. *Mater. Chem. Phys.* **232**, 109–120 (2019).
67. Long, Y. K., Xiao, L. & Cao, Q.-H. Co-polymerization of catechol and polyethylenimine on magnetic nanoparticles for efficient selective removal of anionic dyes from water. *Powder Technol.* **310**, 24–34 (2017).
68. Santhana Krishna Kumar, A., Kalidhasan, S., Rajesh, V. & Rajesh, N. A meticulous study on the adsorption of mercury as tetrachloromercurate (II) anion with trioctylamine modified sodium montmorillonite and its application to a coal fly ash sample. *Ind. Eng. Chem. Res.* **51**, 11312–11327 (2012).
69. Gupta, H. & Singh, S. Kinetics and thermodynamics of phenanthrene adsorption from water on orange rind activated carbon. *Environ. Technol. Innov.* **10**, 208–214 (2018).
70. Kumar, A. & Gupta, H. Activated carbon from sawdust for naphthalene removal from contaminated water. *Environ. Technol. Innov.* **20**, 101080 (2018).
71. Li, H.-L., Ying, R., Tay, J., Tsang, S.-H. & Zhen, X. Tong Teo, E.H. Controllable synthesis of highly luminescent boron nitride quantum dots. *Small* **48**, 6491–6499 (2015).

ACKNOWLEDGEMENTS

We would like to thank the Ministry of Science and Technology (MOST 110-2811-M110-512) for the financial support of this study and also this research was funded by the Foundation for Polish Science POIR.04.04.00-00-14E6/18-00 under the project "Fly ashes as the precursors of functionalized materials for applications in environmental engineering, civil engineering, and agriculture" carried out within the TEAM-NET program.

AUTHOR CONTRIBUTIONS

A.S.K.K.: Conceptualization, Methodology, Formal analysis, Data curation, Investigation, Writing-original draft, [(J.W., J.M., N.R.: Writing—review and editing)], W.-L.T.: Investigation, Resources, Funding acquisition, Writing—review and editing, Project administration, T.B.: Writing-review and editing, Funding acquisition. All the authors are discussed the results and commented on the manuscript.

COMPETING INTERESTS

The authors declare no competing interests.

ADDITIONAL INFORMATION

Supplementary information The online version contains supplementary material available at https://doi.org/10.1038/s41545-022-00175-0.

Correspondence and requests for materials should be addressed to Wei-Lung Tseng, N. Rajesh or Tomasz Bajda.

Reprints and permission information is available at http://www.nature.com/reprints

Publisher's note Springer Nature remains neutral with regard to jurisdictional claims in published maps and institutional affiliations.